

Measurement of parallel blade–vortex interaction at low Reynolds numbers

David Rival · Roland Manejev · Cam Tropea

Received: 5 July 2009 / Revised: 1 December 2009 / Accepted: 4 December 2009 / Published online: 5 January 2010
© Springer-Verlag 2010

Abstract In this study parallel blade–vortex interaction for a Schmidt-propeller configuration has been examined using particle image velocimetry (PIV). This tandem configuration consists of a leading airfoil (forefoil), used to generate a vortical wake of leading-edge vortices (LEVs) and trailing-edge vortices (TEVs) through a pitching or plunging motion, and a trailing airfoil (hindfoil), held fixed with a specified angle of attack and vertical spacing in its wake. The hindfoil incidence (loading) and not the vertical spacing to the incoming vortical wake has been found to dictate the nature of the interaction (inviscid vs. viscous). For cases where the vortex–blade offset is small and the hindfoil is loaded, vortex distortion and vortex-induced separations are observed. By tracking the circulation of the LEV and TEV, it has been found that the vortices are strengthened for the tandem arrangement and in certain cases dissipate quicker in the wake when interacting with the hindfoil. Time-averaged forces obtained using a standard control-volume analysis are then obtained and used to evaluate these vortex-interaction cases. A subsequent analysis of the varying pressure distribution over the suction side of the hindfoil is performed by integrating the Navier–Stokes equations through the velocity field. This allows for a direct comparison of the vortex-induced loading for the various configurations.

D. Rival (✉) · R. Manejev · C. Tropea
Institute of Fluid Mechanics and Aerodynamics,
Technische Universität Darmstadt, Darmstadt, Germany
e-mail: rival@aero.tu-darmstadt.de; d.rival@sla.tu-darmstadt.de;
rival@mit.edu

Present Address:
D. Rival
Postdoctoral Associate in Mechanical Engineering at MIT,
Darmstadt, Germany

1 Introduction

The interaction between a vortex and an arbitrary body can be characterized by the orientation of the vortex (parallel, streamwise or normal) as well as the proximity at which the vortex passes, i.e. inviscid versus viscous interaction. For a viscous interaction, Doligalski et al. (1994) describes the process as an abrupt eruption of the boundary layer induced by the passing or impact of a vortex. A large body of analytical, numerical and experimental studies exists in the literature for such interactions and have been reviewed in great detail by Rockwell (1998). Parallel blade-vortex interaction, a subset of vortex–body interactions examined extensively by Wilder and Telionis (1998), occurs in a wide spectrum of applications and Reynolds numbers. For high Reynolds-number applications ranging from rotorcraft to wind turbines, it is often adequate to use an inviscid treatment as in Yao and Liu (1998). However, at the other end of the spectrum, i.e. miniaturized flapping drones referred to as micro air vehicles (MAVs), large separations are inevitable, as described in Mueller (2001). For such cases, the dynamic pressures are extremely low, i.e. $\Delta p = \mathcal{O}(10 \text{ Pa})$, such that the integration of fast-response miniaturized pressure sensors in small wind-tunnel models becomes impractical. Similarly, direct force measurements are challenging since one has to separate the aerodynamic and inertial forces, see Rival et al. (2009). Therefore, a shift to velocity field measurements such as PIV is often necessary to quantitatively examine such interactions and obtain the unsteady loadings at these low Reynolds numbers. In fact, in stark contrast to pressure or direct force measurements, the accuracy of PIV remains insensitive to flow velocity magnitude, as discussed by van Oudheusden et al. (2007).

The configuration used in this study to examine parallel blade–vortex interaction was originally referred to as a wave propeller, developed by Schmidt (1965), as it was conceived to extract vortical energy from the upstream foil (wave generator) and subsequently use this residual energy to generate thrust on the static hindfoil (propeller). Since its original development this configuration has been investigated experimentally and numerically by Jones and Platzer (1999). Recently, a similar arrangement has been investigated by Beal et al. (2006) in the context of biomimetic propulsion in vortex wakes, i.e. fish swimming in high-energy environments such as streams and rivers. In such cases, the details of the vortical interaction at the hindfoil leading edge are of great importance to thrust generation due to the development of low-pressure regions at the front of the body, a phenomenon known as leading-edge suction. In the present study, blade–vortex interactions for non-zero incidence kinematics analogous to the tandem-configuration associated with lift and thrust generation in dragonfly flight are investigated in detail, see Thomas et al. (2004).

2 Load evaluation

Since the measurement of transient loads via direct force measurements or pressure taps is very challenging at such low dynamic pressures, control-volume analyses and pressure-integrations of the respective velocity fields were performed instead. The former method provides a global measurement of the blade–vortex interaction whereas the latter the spatial and temporal evolution of the suction spike over the hindfoil. In the following, these two methodologies are introduced and discussed.

2.1 Control-volume analysis

A standard control-volume analysis was used, similar to the one described by van Oudheusden et al. (2007) and Jardin et al. (2009), which allowed for both a time-resolved (12 or 24 phases per cycle) and time-averaged comparison of the various configurations. Both lift (C_l) and drag (C_d) coefficients were obtained from the force vector:

$$\mathbf{F}(t) = -\rho \iiint_V \frac{\partial \mathbf{V}}{\partial t} dV - \rho \iint_S \mathbf{V}(\mathbf{V} \cdot \mathbf{n}) dS - \iint_S p \mathbf{n} dS + \iint_S (\bar{\tau} \cdot \mathbf{n}) dS, \quad (1)$$

where \mathbf{n} is the normal vector to the control surface S bounding control volume V , ρ the fluid density, \mathbf{V} the flow velocity vector, p the pressure and $\bar{\tau}$ the viscous stress tensor. The viscous term was obtained from the velocity field but was found to have a negligible contribution to the

forces. The pressure term played a significant role in the near-wake control-volume analysis and was evaluated using the steady Bernoulli relationship on the top and bottom control surfaces where the flow was inviscid, while the pressure over the rear surface was integrated using equation (2). Finally, the unsteady term (volume integral) was neglected in this study since large shadows limited the accuracy of the data within the volume. Nevertheless, at this relatively low reduced frequency ($k = 0.25$), the authors have found that the convective term was dominant at nearly all time steps except at those with the presence of strong vortical structures such as the LEV. At instances when the LEV or TEV passed through the control volume, discrepancies to the instantaneous direct force measurements on the order of 5% were observed when using the quasi-steady control-volume analysis. Similar results have been presented by Kat et al. (2008) for the immediate wake of a square cylinder. Furthermore, when determining the average forces for a periodic motion, as presented in Tables 1 and 2, the unsteady term cancels out over the cycle. In other words, the unsteady term is not required to determine the mean lift and drag forces.

A schematic depicting the position of both single and combined control volumes is found in Fig. 1a. Note the single control volume was used to validate the method with direct force measurements (see Fig. 2; Table 1) whereas the combined control volume was used for all tandem arrangements, encompassing both fore- and hindfoils. Similar to the technique used by van Oudheusden et al. (2007), the corresponding uncertainty in the time-averaged lift and drag coefficients was determined by varying the control-volume surfaces and observing the sensitivity of the resulting force coefficients. The uncertainty for these time-averaged lift and drag coefficients could then be estimated to be $\Delta C_l = \Delta C_d = \pm 0.02$.

2.2 Pressure integration

Due to the inherent boundary-layer separation occurring in blade–vortex interactions, traditional attached-flow aerodynamics based on potential flow solutions cannot be used. Rather the rearrangement and integration of the Navier–Stokes equations (in both x- and y-directions) can provide information on the relevant pressure fields over the target airfoil:

$$\iint_S \nabla p dS = \iint_S \left[\mu \Delta \mathbf{V} - \rho \left(\frac{\partial \mathbf{V}}{\partial t} + \mathbf{V} \cdot \nabla \mathbf{V} \right) \right] dS, \quad (2)$$

where μ is the dynamic viscosity. Such an analysis has been used in the past for the study of blade–vortex interaction by Wilder and Telionis (1998). Again, as mentioned earlier for the control-volume analysis, the estimated strength of the

Table 1 Validation of control-volume analysis technique for mean lift and drag forces; note large discrepancy in pure-plunge 8° (single) case since direct force measurements taken from different facility, see Ol et al. (2009)

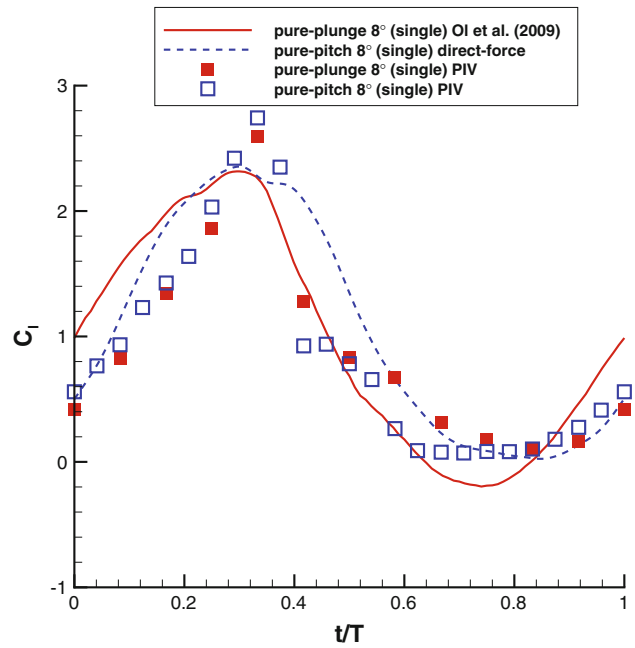
| Case | C_l (direct force) | C_l (PIV) | C_d (direct force) | C_d (PIV) |
|-------------------------|----------------------|-------------|----------------------|-------------|
| Static 8° | 0.86 | 0.79 | 0.09 | 0.08 |
| Static 20° | 0.84 | 0.88 | 0.33 | 0.28 |
| Pure-plunge 8° (single) | 0.96 | 0.88 | — | 0.09 |

Table 2 Comparison of mean lift and drag coefficients for the various cases

| Case | C_l (PIV) | C_d (PIV) |
|---|-------------|-------------|
| Pure-plunge 8° (single) | 0.88 | 0.09 |
| Pure-pitch 8° (single) | 0.91 | 0.18 |
| Pure-pitch 8° ($h/c = 0, 8^\circ$) | 1.66 | 0.32 |
| Pure-plunge 8° ($h/c = -0.25, 0^\circ$) | 0.93 | 0.13 |
| Pure-plunge 8° ($h/c = -0.25, 8^\circ$) | 1.60 | 0.15 |
| Pure-plunge 8° ($h/c = -0.5, 0^\circ$) | 0.91 | 0.14 |
| Pure-plunge 8° ($h/c = -0.5, 8^\circ$) | 1.35 | 0.15 |

unsteady term in the pressure integration was found to be much smaller than the convective contribution. By integrating the Navier–Stokes equations first vertically down with equation (2), i.e. from points A to B from a point outside of the wake where the integration constant (at point A) can be obtained through Bernoulli, the pressure near the hindfoil leading edge can be quantified. Subsequently, an integration across the streamwise direction, i.e. from points B to C, is used to determine the pressure distribution over the hindfoil and thus describe the nature of the blade–vortex interaction. This integration path and the corresponding pressure field are shown in Fig. 1b. The numerical integrations were performed using a forward-differencing scheme, as described by Raffel et al. (2007).

The dimensionless pressure distribution obtained along line B–C was not extracted directly on the suction side of the airfoil in order to avoid integration through the optical boundary layer. The maximum deviations of the B–C

**Fig. 2** Comparison of lift forces extracted from control-volume analysis with direct force measurements; note direct force measurements for pure-plunge 8° (single) case taken from Ol et al. (2009)

integration line from the airfoil surface occur at the leading- and trailing edges are $y/c \approx 0.12$ for $\alpha_H = 0^\circ$ and $y/c \approx 0.08 – 0.22$ for $\alpha_H = 8^\circ$. Once outside of the optical boundary layer, the sensitivity of the integration path was found to be minor. In order to test the level of error propagation using the pressure-integration technique,

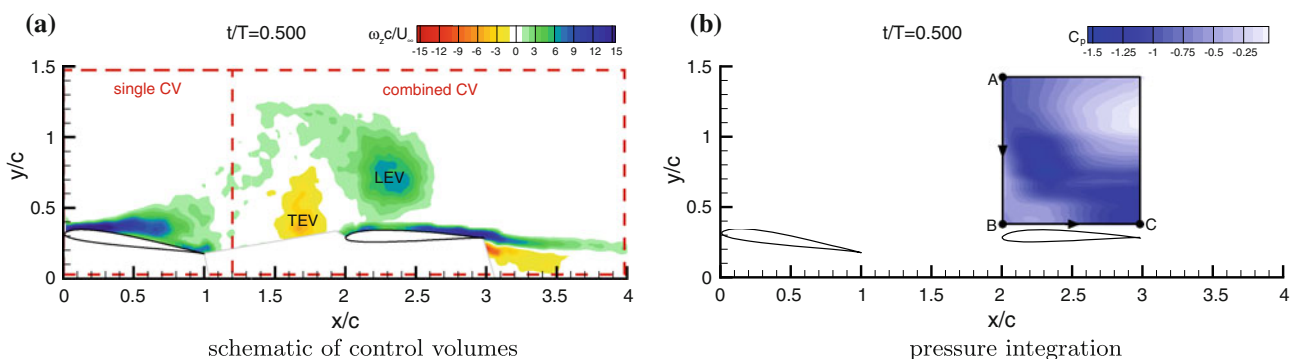
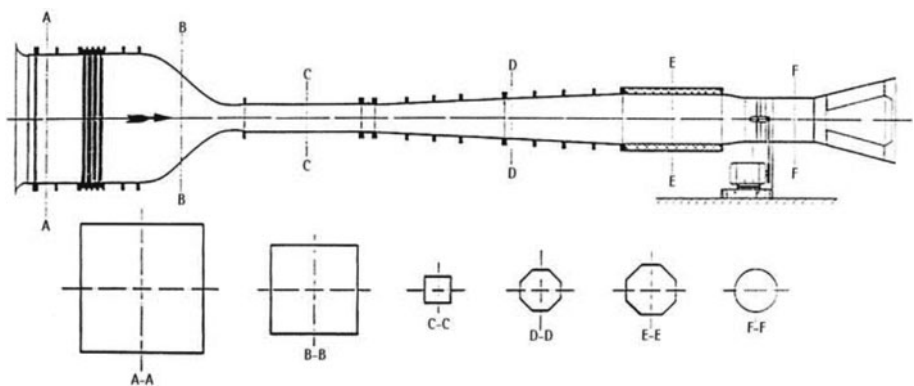
**Fig. 1** Schematics of **a** both single and combined control volumes superimposed on top of vorticity field, and **b** pressure integration over hindfoil for pure-plunge 8° ($h/c = -0.5, 0^\circ$) case; note integration follows path A to B to C

Fig. 3 Schematic of wind tunnel; note intake (A–A) and test section (C–C) cross-sections



the pressure distributions were calculated by integrating vertically down toward the trailing edge and then horizontally from C to B ending at the leading edge. The maximum deviation in the pressure coefficient for all cases was approximately $C_p = \pm 0.1$. Despite the assumption of a quasi-steady flow and the error propagation associated with the pressure integration, the calculated pressure distributions over the hindfoil provide the necessary qualitative insight into the nature of the blade–vortex interaction at these low Reynolds numbers.

3 Experimental setup

This study was carried out in the Eiffel-type wind tunnel at the Institute of Fluid Mechanics and Aerodynamics (TU Darmstadt). The test section of this low-speed wind tunnel has a cross section of 45 by 45 cm and a length of 2 m. Furthermore, the tunnel has a contraction ratio of 24:1 with five turbulence filters in the settling chamber and produces turbulence levels on the order of 1.0% at these low test speeds. A schematic of the wind tunnel is shown in Fig. 3. The free-stream velocity was controlled via closed-loop control, with the tunnel speed input obtained from a hot-wire anemometer (Dantec Dynamics A/S type 55P11) positioned at the entrance of the test section. The hot-wire anemometer was calibrated for each new set of measurements using a miniature vane anemometer.

Both carbon-fiber SD7003 wall-spanning airfoils selected for the wind-tunnel measurements were asymmetric SD7003 profiles with $0.09c$ maximum thickness. The SD7003 profile was used since it demonstrates relatively good performance at transitional Reynolds numbers, see Selig et al. (1995). Another attractive feature in using this profile is the substantial experimental database available in the open literature such as in Ol et al. (2009).

Four linear motors of type LinMot PS01-48x240F-C were used to drive the pitch/plunge motions. External position sensors were mounted on the motor units for higher positional accuracy, allowing for a displacement

accuracy of ≤ 0.5 mm and a dynamic angle-of-attack accuracy of less than 0.5° . All experiments were performed at a physical frequency of $f = 2.5$ Hz equivalent to $k = 0.25$, where the reduced frequency is defined as:

$$k = \frac{\pi f c}{U_\infty}, \quad (3)$$

where f is the pitching/plunging frequency, c the airfoil chord and U_∞ the free-stream velocity. At this reduced frequency, a clearly defined vortical wake is produced, as identified in Rival and Tropea (2009), which in turn is ideal for the study of blade–vortex interaction at this low Reynolds number of $Re = 30000$.

A commercial PIV system was used in this study (Dantec Dynamics A/S) and consisted of a Nd:YAG ($\lambda = 532$ nm) Litron dual-cavity laser with a maximum power output of 135 mJ per cavity and two 10-bit FlowSense 2 M CCD cameras each with a $1,600 \times 1,200$ pix resolution. Due to the large imaging field required, 60 mm

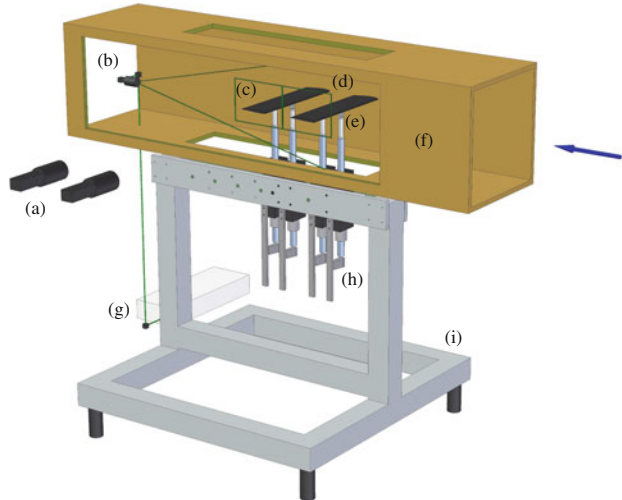


Fig. 4 Experimental setup in wind tunnel with flow direction from right-to-left: a CCD cameras, b beam expander, c PIV image frames, d wall-spanning carbon-fiber profiles, e embedded piezo-electric force sensors, f test-section, g laser head, h linear motors with linkage system and i base structure

f/2.8 Nikkor lenses were used. The Schmidt-propeller configuration in the wind tunnel with PIV setup is shown in Fig. 4. For a detailed description of the experimental rig, the SD7003 profile, as well as the wind tunnel itself, please refer to Rival et al. (2009).

PIV image pairs were sampled at 15 Hz allowing for 6 phases to be recorded per cycle at $k = 0.25$. In order to construct the ensemble velocity fields of 12 phases per cycle (24 in the case of pure-pitch), two (or four) staggered sets with 100 images per phase were ensemble-averaged. In all cases, the first two starting cycles were removed from all ensembles. Each camera imaged a field corresponding to $x/c = 2$ and $y/c = 1.5$, with a resolution of 800 pix/c (6.7 pix/mm). Reflections on the model surface were strongest at the bottom of the stroke where a region $0.04c$ normal to the airfoil surface was deemed to be unreliable. Shadows and strong reflections on the pressure (lower) side required masking. Parallax effects were strongest at the top of the stroke and at this position were responsible for hiding a region $0.03c$ normal to the airfoil surface. The vector fields were calculated using an adaptive correlation with 32×32 pix interrogation windows and a 50% overlap. A 3×3 filter was used to lightly smooth the vector fields in order to more clearly define the vortical structures in the wake. A local neighborhood validation using a 9×9 moving-average filter and an acceptance factor of 0.2 was employed to eliminate outliers. This, however, also had the effect of smoothing the velocity gradients, thereby thickening the shear layers.

The accuracy of the vector fields was estimated to lie well below 2% of the free-stream velocity ($U_\infty = 3.75$ m/s) for all cases, assuming a maximum sub-pixel interpolation accuracy of 0.2 pix, see Raffel et al. (2007). Due to the coarse measurement resolution and the low vector overlap (50%), neighboring vectors were assumed to be weakly correlated. Subsequently, the vorticity and circulation could be estimated to have uncertainties of $\Delta\omega c/U_\infty = \pm 0.5$ and $\Delta\Gamma/U_\infty c = \pm 0.05$, respectively. When calculating the circulation various threshold values were tested. For a threshold of 0.1 dimensionless vorticity, a change in circulation of under 1% was measured. The largest differences were found for the TEV late in the stroke where the vortices were most dissipated. Integrating over the windows without a threshold or using large threshold values (up to 0.5) were also tested and were deemed to not have a significant impact on the results. Therefore, a threshold of zero was chosen.

The vortex trajectories were determined by tracking the point of highest vorticity of the respective LEV and TEV cores in time. The spatial resolution of this manual-tracking method is approximately $x/c = y/c = \pm 0.05$.

4 Parameter space

As mentioned previously, the Schmidt-propeller configuration used in this study consisted of an oscillating forefoil and a static hindfoil positioned at $x/c = 2$ in its wake (distance measured between quarter-chord positions). The forefoil was oscillated with a so-called *pure-plunge* motion based on a simple harmonic motion:

$$h(t) = h_o \cos(2\pi ft), \quad (4)$$

where h is the time-dependent plunge position, h_o the plunge amplitude and f the frequency of the period. A geometric angle of attack of 8° was used since at this reduced frequency of $k = 0.25$ strong LEV–TEV vortex pairs were found to be repeatedly shed into the wake. The plunge amplitude of $h_o = 0.5c$ was also fixed. An equivalent pure-pitch motion with a mean angle of attack of 8° and pitch amplitude of 14.1° was tested and found to produce a very similar vortex wake, yet slightly more compact than that of the pure-plunge motion. Since direct force measurements were only available for the pure-pitch case, these analogous tests were invaluable for validating the control-volume method presented in Sect. 5.4. For a detailed comparison of these two motions please refer to Rival and Tropea (2009). The hindfoil had three static vertical offsets (h/c) relative to the forefoil centerline. The first position corresponded to the center position of the forefoil's stroke ($h/c = 0$), the second position was at the quarter-stroke position ($h/c = -0.25$) and the third position at bottom-dead-center ($h/c = -0.5$). The angle of attack of the hindfoil was varied between $\alpha_H = 0^\circ$ and $\alpha_H = 8^\circ$.

5 Results

5.1 Trajectories and convective velocities

The wakes of two single-airfoil reference cases and five tandem test cases have been captured, where the kinematics of the forefoil are based on the studies in Rival et al. (2009), referred to as *pure-plunge* 8° (single) and *pure-pitch* 8° (single). The angle of attack (α_H) and relative positioning (h/c) of the hindfoil to the centerline are given in brackets in the corresponding figure legends. Cases with $\alpha_H = 0^\circ$ are referred to as *unloaded* cases since the hindfoil at this incidence produces negligible lift. Conversely, cases with $\alpha_H = 8^\circ$ are considered *loaded* since the hindfoil at this incidence generates considerable lift. However, for the latter case, the flow is on the verge of stall and is therefore very sensitive to the vortex–blade interaction examined here.

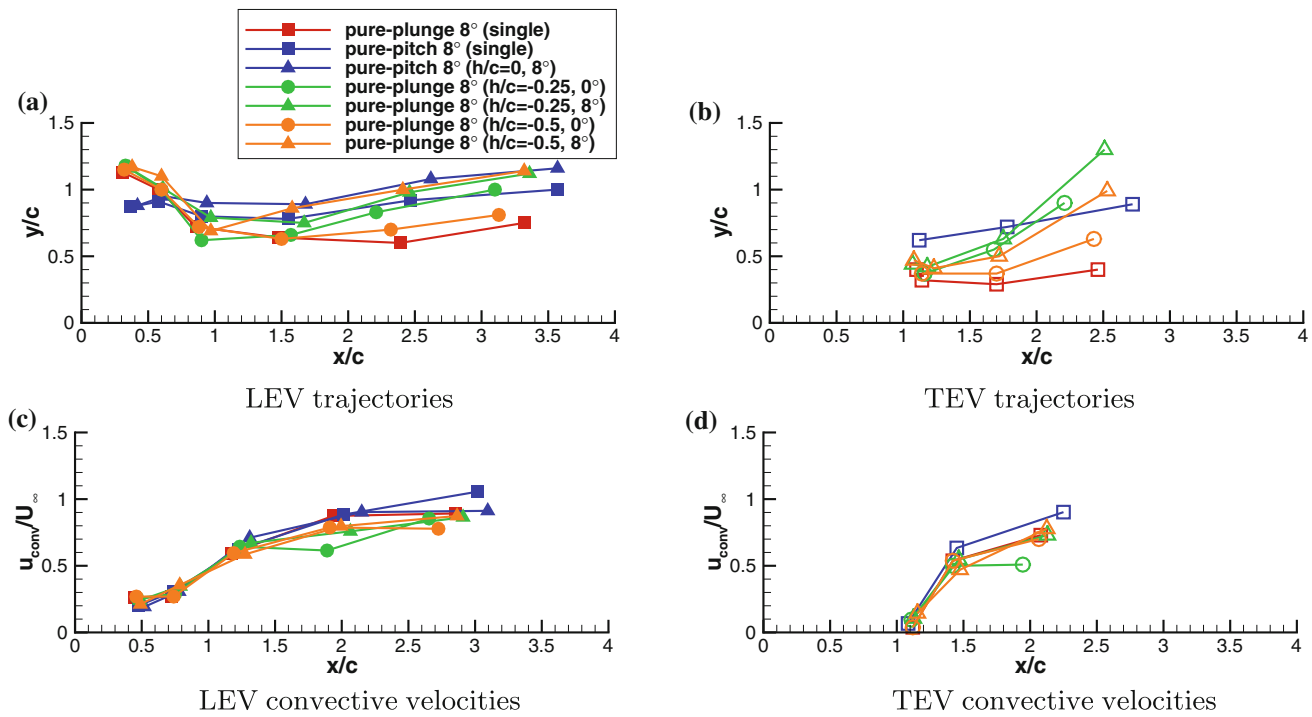


Fig. 5 Measured trajectories and convective velocities of LEV and TEV cores for the various single-airfoil and tandem-airfoil configuration; note h/c refers to vertical orientation of hindfoil

By tracking the trajectories of the wake vortices, see Fig. 5a, b, the nature of the blade–vortex interaction for the various cases can be examined. Here, the effect of the hindfoil circulation - proportional primarily to the hindfoil angle of attack α_H - causes the shed vortices to shift upward in the wake as they travel downstream. Subsequently, the convective velocities of these vortices have been extracted, as shown in Fig. 5c, d. Here, the convective velocities show very similar trends, with the exception of the pure-plunge 8° ($h/c = -0.25, 0^\circ$) case where the TEV impacts the hindfoil leading edge directly. In this case, the LEV passes much closer to the airfoil surface such that the vortex core distance to the surface is $y/c \approx 0.25$ instead of $y/c \approx 0.5$ for $h/c = -0.5$. This close proximity in turn decelerates the vortex due to ground effect, i.e. a figurative image vortex below the hindfoil's surface, a phenomenon described by Doligalski et al. (1994). For this unloaded case, no separation is induced at the leading edge. Conversely, for the equivalent loaded blade interaction, the separated region at the leading edge shields the LEV from the wall's dissipative effects. Wilder and Telionis (1998) came across this shielding effect of the leading-edge shear layer in their studies when comparing the vortex–blade interactions between both unloaded and loaded cases. In the following section, the dissipation due to vortex interaction with the hindfoil has been quantified and tracked over time.

5.2 Vortex circulation

In Fig. 6, the temporal evolution of both LEV and TEV circulation has been plotted over the cycle. As reported by Rival et al. (2009), the LEV is found to reach its maximum

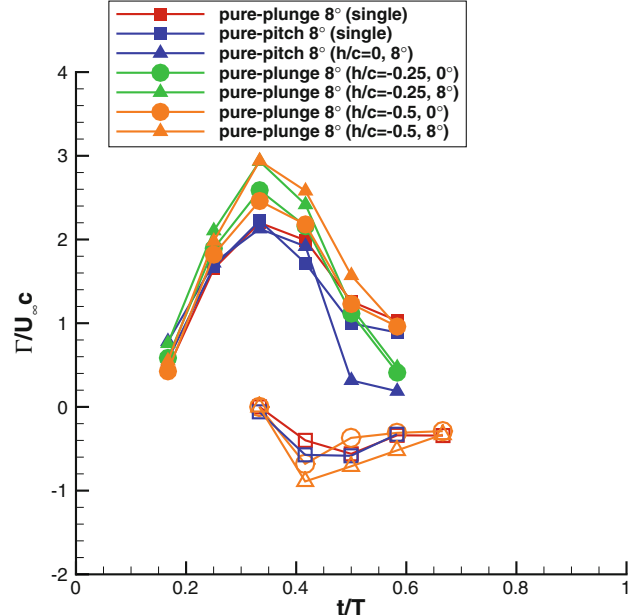


Fig. 6 Development of LEV and TEV circulation as a function of period for the various single-airfoil and tandem-airfoil configurations; note solid and hollow symbols represent LEVs and TEVs, respectively

circulation just before pinch-off from the leading-edge shear layer. The general peak-shape of the LEV circulation curve correlates well with the peak in the lift distribution presented in Fig. 2, albeit with a slight phase delay. Of interest here for the tandem configurations is the substantial strengthening of the LEV in comparison with the single-airfoil reference case, particularly for the cases with $\alpha_H = 8^\circ$. This strengthening is due to the circulation of the hindfoil in the forefoil's wake, which has the effect of increasing the size of the developing LEV. In turn, the TEV is strengthened by the induction of the LEV as it passes over the trailing edge. After peak LEV circulation at $t/T = 0.333$, the vortex strength decreases rapidly due to several influences. This rapid deterioration in circulation can be attributed to viscous dissipation, three-dimensional break-up of the vortex and interaction with the hindfoil. When compared to the single-airfoil case, there is a more dramatic drop in circulation between $t/T = 0.5$ and $t/T = 0.583$ for the tandem configurations with $h/c = -0.25$. For these cases, the vortex passes very closely over

the hindfoil surface and therefore the viscous dissipation is much stronger, as described by Wilder and Telionis (1998). This interaction can be seen in Figs. 7 and 8.

5.3 Vortex-induced separation

For certain cases when the hindfoil is loaded and thus near its stall limit, i.e. $\alpha_H = 8^\circ$, a vortex-induced separation occurs when the TEV passes close over the hindfoil leading edge. The TEV with its counter-clockwise rotation generates an upwash at the leading edge. This in turn induces a boundary-layer separation analogous to dynamic stall leading to the roll-up of a clockwise-oriented LEV. This effect could be best observed for the pure-plunge 8° ($h/c = -0.5, 8^\circ$) case, as shown in Fig. 7b. This stark contrast between unloaded ($\alpha_H = 0^\circ$) and loaded ($\alpha_H = 8^\circ$) cases has also been observed in the blade–vortex interaction studies of Wilder and Telionis (1998).

In Fig. 8, a similar comparison between unloaded and loaded blade–vortex interaction can be made, albeit the vertical spacing of the hindfoil is such that the TEV

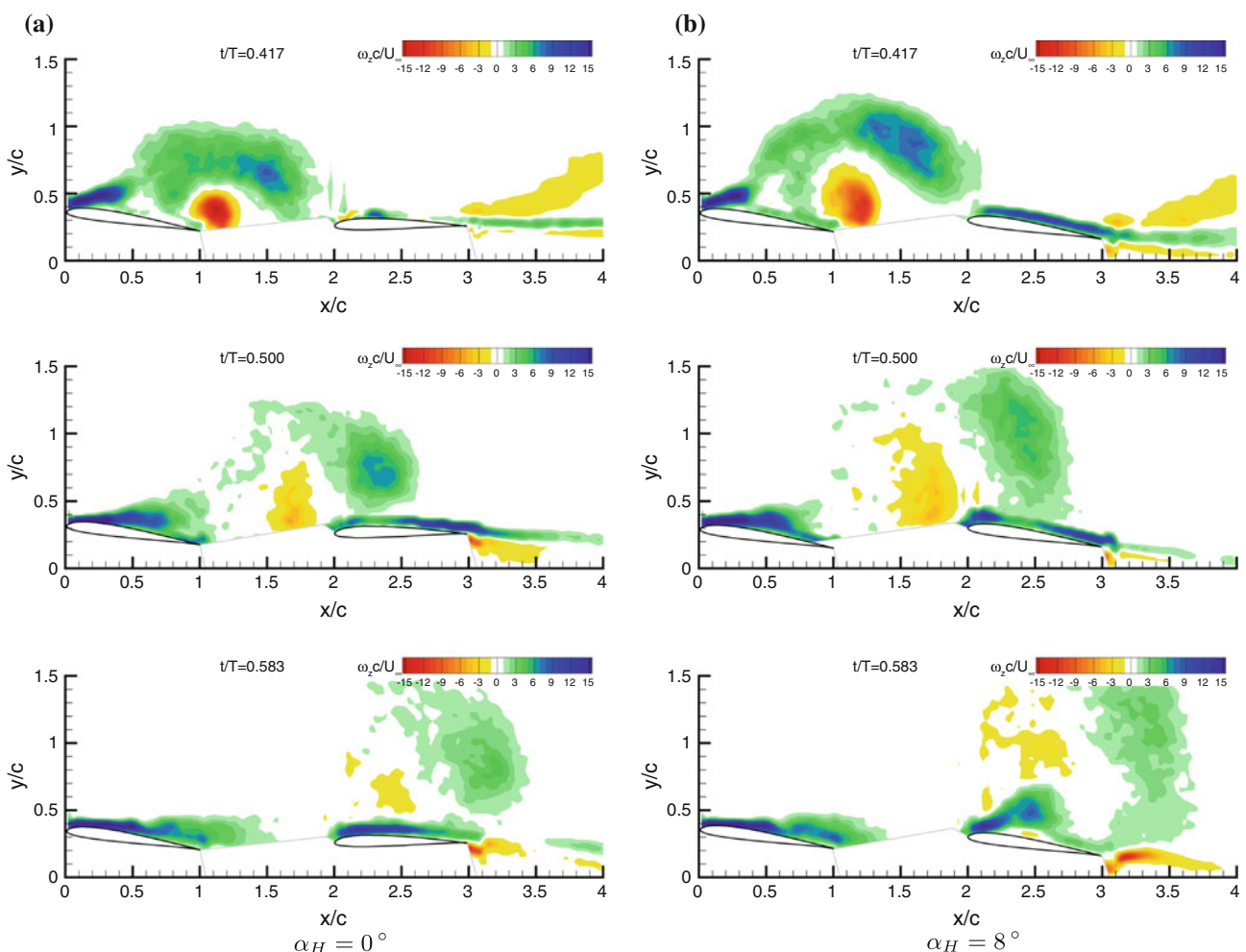


Fig. 7 Comparison of blade–vortex interaction between unloaded and loaded cases; **a** $h/c = -0.5$ and $\alpha_H = 0^\circ$, and **b** $h/c = -0.5$ and $\alpha_H = 8^\circ$

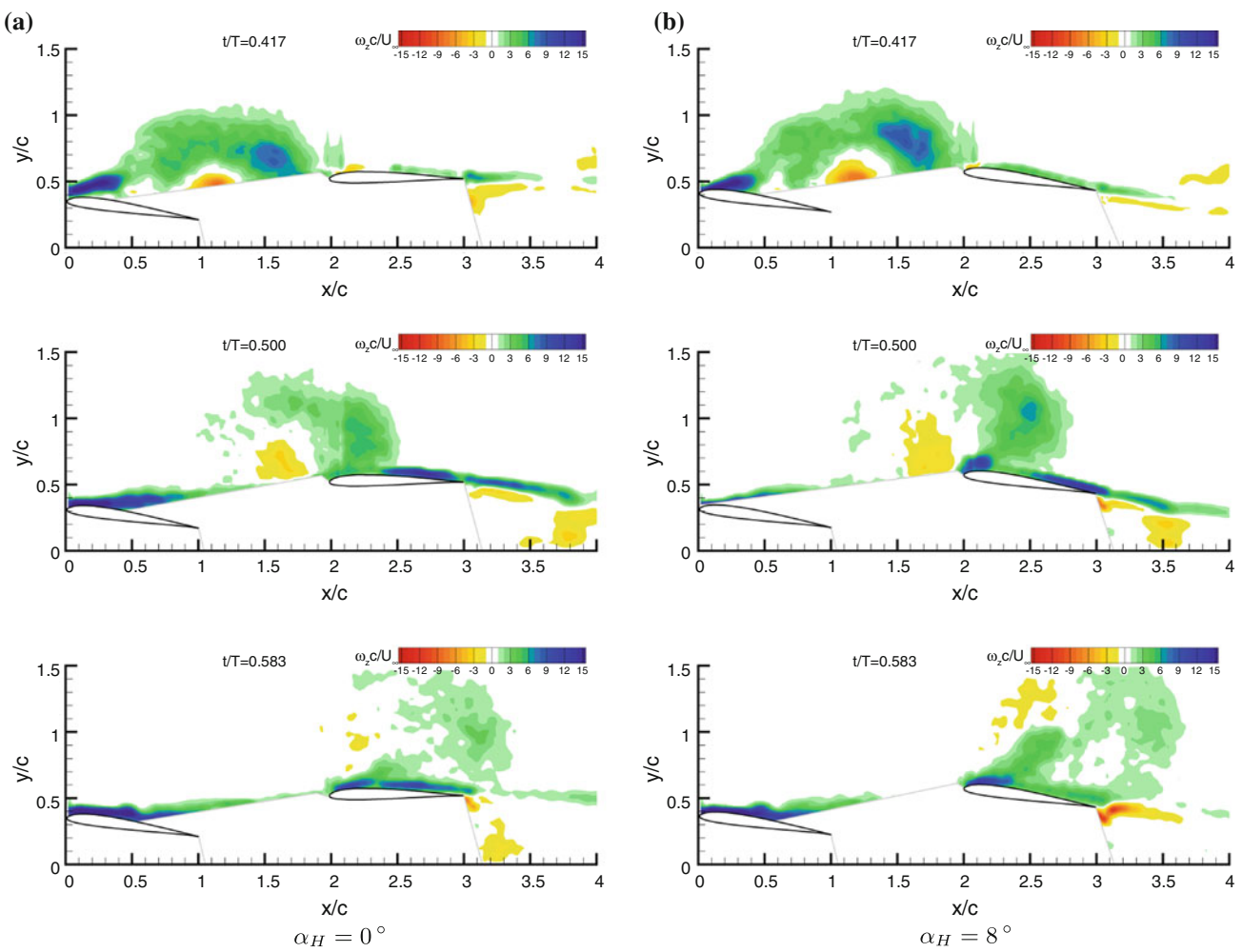


Fig. 8 Comparison of blade–vortex interaction between unloaded and loaded cases; **a** $h/c = -0.25$ and $\alpha_H = 0^\circ$, and **b** $h/c = -0.25$ and $\alpha_H = 8^\circ$

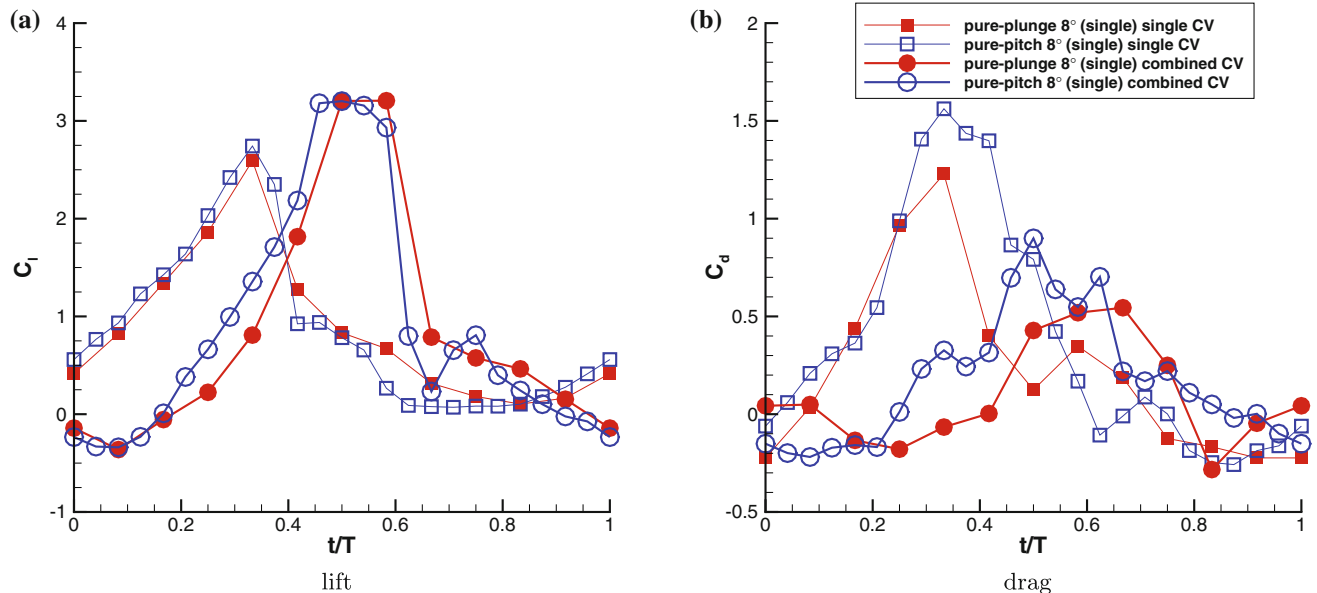


Fig. 9 Variation of lift **a** and drag **b** using two different control volumes (see Fig. 1a; note symbols represent position of measurement phases over the period)

impacts the leading edge and dissipates more rapidly than for $h/c = -0.5$. In Fig. 8a, leftover portions of the TEV pass over both surfaces of the hindfoil into the wake. Before the occurrence of this strong viscous interaction ($t/T = 0.417$ and $t/T = 0.5$), the approaching TEV clearly induces a separation at the hindfoil leading edge for the pure-plunge 8° ($h/c = -0.25, 8^\circ$) case. When comparing Figs. 7 and 8 with each other, one can observe very strong similarities between the unloaded and loaded cases suggesting that the dominant parameter affecting the vortical interaction is the hindfoil incidence (α_H) and not the vertical offset (h/c).

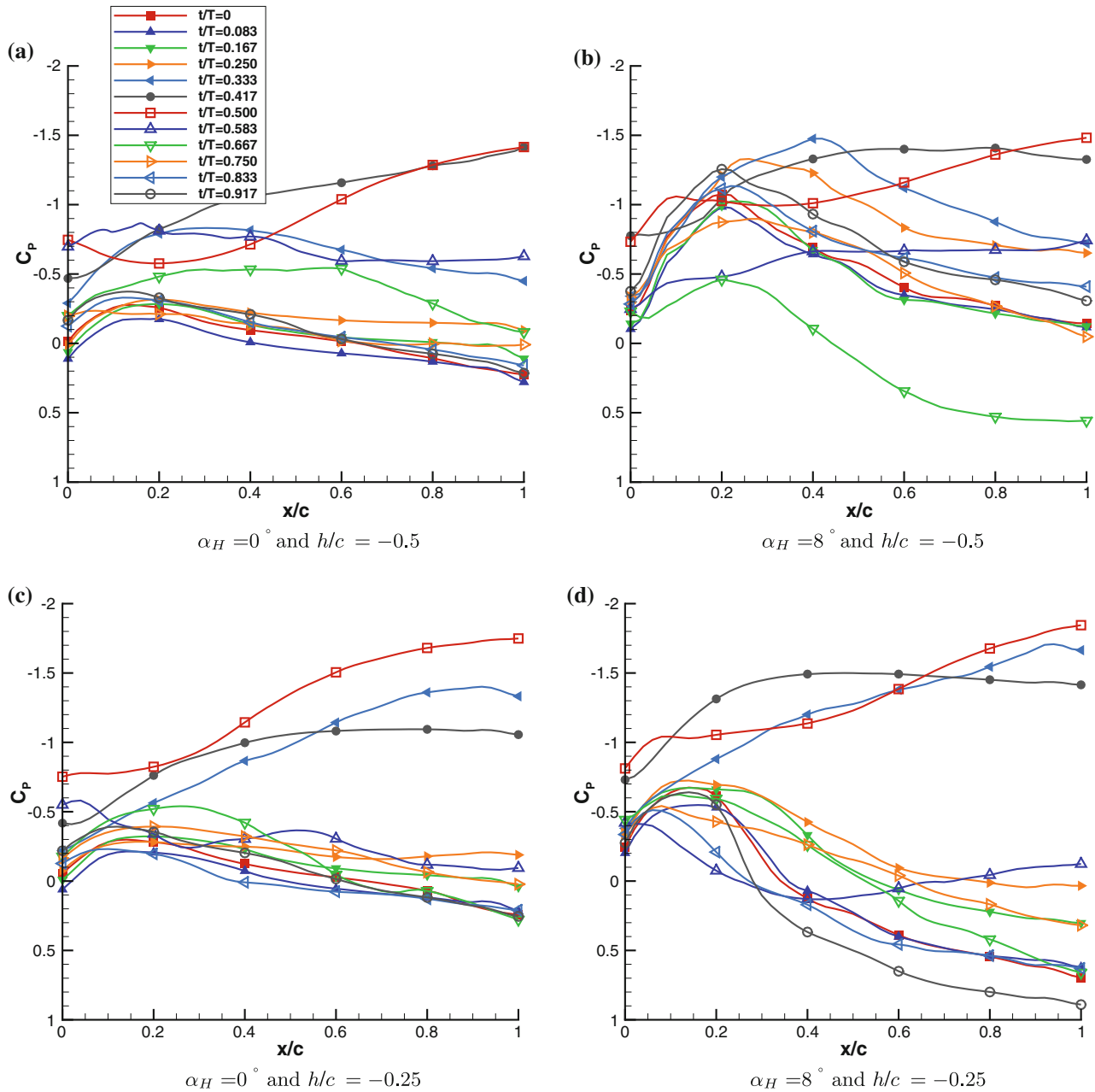


Fig. 10 Pressure distributions over hindfoil surface for the various tandem configurations demonstrating blade–vortex interaction

5.4 Control-volume analysis

In Table 2, a summary of the combined lift and drag coefficients for the various tandem configurations is presented. Interestingly, the tandem configurations show combined values of lift similar to levels of two separate airfoils (pure-plunge plus static), see Table 1 for values. This suggests that any increase in lift due to vortex interaction is canceled out by the subsequent vortex-induced separation. However, when examining drag for the pure-pitch 8° ($h/c = 0, 8^\circ$) case, a substantial increase can be observed. Conversely for the other Schmidt cases drag is

reduced, albeit by a very minor amount. This net thrust increase on the hindfoil can be explained by vortical interaction at the leading edge, i.e. leading-edge suction, as first measured by Schmidt (1965).

Due to the inherent shadow between fore- and hindfoils, it was not possible to separate the individual forces from each airfoil. Furthermore, a time-resolved examination of the blade–vortex interaction using the quasi-steady, combined control-volume analysis was restrictive since the wake velocity information from the forefoil arrived relatively late at the downstream control surface, thus distorting the shape of the force curves in time. In Fig. 9, the peak in lift and drag using the combined control volume is clearly shifted by $t/T \approx 0.25$ to the right when compared to curves obtained using the single control volume in Fig. 2. This time delay between the single and combined control volumes corresponds to the time for the wake information to be convected to the rear control surface at the free-stream velocity.

5.5 Pressure distributions

In Fig. 10, the evolution of the pressure distribution over the hindfoil is plotted for two angles of attack. Note $t/T = 0$ and $t/T = 0.5$ correspond to the top and bottom of the forefoil stroke, respectively. In both instances, one can see that a strong suction occurs at $0.333 \leq t/T \leq 0.5$, corresponding to the approaching TEV shown in Figs. 7 and 8. The first wave of suction is associated with the passing vortical layer from the trailing edge (counter-clockwise), which in turn generates an upwash on the hindfoil. For the $\alpha_H = 8^\circ$ case, seen in Fig. 10b, a strong vortex-induced separation is generated at the hindfoil's leading edge, corresponding to the proximity of the TEV at the leading edge ($t/T = 0.5$). The overall increase in leading-edge suction over this period accounts for the reduction in net drag. The net lift as reported in Table 2 however, is unchanged when compared to the individual cases and can be explained by the increase in separation once the LEV and TEV have passed downstream. After the convection of the vortex pair, the flow gradually returns to its quasi-steady state by $t/T = 0.75$.

6 Conclusions

The blade–vortex interaction in a Schmidt-propeller configuration has been investigated using PIV. Vortex trajectories, velocities and circulation, combined with time-averaged lift and drag forces as well as pressure distributions over the hindfoil, have all been extracted from the respective velocity fields. The main parameter influencing the nature of the vortical interaction on the hindfoil was

identified as the incidence (loading) and not the vertical spacing to the forefoil. For all tandem arrangements, the LEV and TEV circulation on the forefoil was found to be significantly strengthened. However, only in certain cases, the dissipation in vortex circulation was quicker than for the single-airfoil arrangement, suggesting that the blade–vortex interaction is only one of several mechanisms influencing vortical breakdown in the wake. Subsequently, the control-volume analysis has shown that the combined mean lift for the tandem cases is not increased through blade–vortex interaction. However, a combined mean drag reduction is apparent for certain configurations and can be attributed to TEV-induced leading-edge suction on the hindfoil. The spatial and temporal variation in pressure over the hindfoil associated with the passing vortical wake is extracted using the pressure-integration method and provides further insight into the leading-edge suction mechanism.

Acknowledgments This research was supported by the Deutsche Forschungsgemeinschaft (DFG) within the national priority program entitled *Nature-Inspired Fluid Mechanics* (SPP1207, Tr 194/40). The authors would also like to acknowledge the very constructive feedback from the reviewers.

References

- Beal DN, Hover FS, Triantafyllou MS, Liao JC, Lauder GV (2006) Passive propulsion in vortex wakes. *J Fluid Mech* 549:385–402
- Doligalski T, Smith C, Walker J (1994) Vortex interactions with walls. *Ann Rev Fluid Mech* 26:573–616
- Jardin T, Laurent D, Farcy A (2009) Characterization of vortical structures and loads based on time-resolved PIV for asymmetric hovering flapping flight, Vol 46(5), doi:[10.1007/s00348-009-0632-7](https://doi.org/10.1007/s00348-009-0632-7)
- Jones KD, Platzer MF (1999) An experimental and numerical investigation of flapping-wing propulsion. In: 37th AIAA Aerospace Sciences Meeting and Exhibit, AIAA-99-0995, Reno, USA
- Kat R, Oudheusden BW, Scarano F (2008) Instantaneous planar pressure field determination around a square-section cylinder based on time-resolved stereo-piv. In: 14th Int Symp on Applications of Laser Techniques to Fluid Mechanics in Lisbon
- Mueller TJ (2001) Fixed and flapping wing aerodynamics for micro air vehicle applications. American Institute of Aeronautics and Astronautics, Inc
- Ol MV, Bernal L, Kang CK, Shyy W (2009) Shallow and deep dynamic stall for flapping low reynolds number airfoils. *Exp Fluids* 46(5):883–901
- Raffel M, Willert CE, Wereley S, Kompenhans J (2007) Particle image velocimetry—a practical guide, 2nd Edn. Springer, Berlin
- Rival D, Tropea C (2009) Characteristics of pitching and plunging airfoils under dynamic-stall conditions. *J Aircr* (in press). doi: [10.2514/1.42528](https://doi.org/10.2514/1.42528)
- Rival D, Prangemeier T, Tropea C (2009) The influence of airfoil kinematics on the formation of leading-edge vortices in bio-inspired flight. *Exp Fluids* 46(5):823–833
- Rockwell D (1998) Vortex–body interactions. *Ann Rev Fluid Mech* 30:199–229
- Schmidt W (1965) Der wellpropeller, ein neuer antrieb fuer wasser-, land- und luftfahrzeuge. *Z Flugwiss Weltraumforsch* 12:472–479

- Selig M, Guglielmo J, Broeren A, Giguere P (1995) Summary of low-speed airfoil data. SoarTech Publications, Virginia Beach
- Thomas ALR, Taylor GK, Srygley RB, Nudds RL, Bomphrey RJ (2004) Dragonfly flight: free-flight and tethered flow visualizations reveal a diverse array of unsteady lift-generating mechanisms, controlled primarily via angle of attack. *J Exp Biol* 207:4299–4323
- van Oudheusden BW, Scarano F, Roosenboom EWM, Casimir EWF, Souverein LJ (2007) Evaluation of integral forces and pressure fields from planar velocimetry data for incompressible and compressible flows. *Exp Fluids* 43(2–3):153–162
- Wilder MC, Telionis DP (1998) Parallel blade–vortex interaction. *J Fluids Struct* 12:801–838
- Yao ZX, Liu DD (1998) Vortex dynamics of blade–blade interaction. *AIAA J* 36(4):497–504